

# Electron Beam-Induced Reduction of Silver on TiO<sub>2</sub> Film

Arantxa Danielle S. MONTALLANA<sup>1</sup>, Lance Tristan Oliver R. PENGSON<sup>2</sup>, Mark D. ILASIN<sup>2</sup>,  
Magdaleno R. VASQUEZ Jr.<sup>2</sup> and Motoi WADA<sup>1</sup>

<sup>1</sup>*Doshisha University, Kyotanabe, Kyoto 610-0321, Japan*

<sup>2</sup>*University of the Philippines, Diliman, Quezon City 1101, Philippines*

(Received 15 September 2023 / Accepted 27 November 2023)

A broad, low-energy electron beam extracted from a multi-cusp plasma source through a pair of mesh electrodes produced metallic silver (Ag) from the Ag compound prepared on the surface of titanium dioxide (TiO<sub>2</sub>) thin films. The TiO<sub>2</sub> films were grown by thermal oxidation of magnetron-sputtered titanium (Ti) films. The reduced metallic Ag formed the Ag-TiO<sub>2</sub> heterostructure. The reduction of the Ag compound was investigated by varying the operating pressure and the electron beam exposure time. The electron energy distribution function was measured using a retarding potential analyzer, while the electron current density measurements were obtained by collecting the electrons passing through the aperture of a shielded Faraday cup. Characterization of the synthesized heterostructure was performed using X-ray diffraction and Raman spectroscopy to check the chemical structure and composition, UV-Vis spectroscopy and 4-point probe to investigate the optoelectronic properties, and electron microscopy to observe the surface morphology of the films. The electron beam characteristics were correlated with the structure and properties of the synthesized Ag-TiO<sub>2</sub> heterostructure.

© 2024 The Japan Society of Plasma Science and Nuclear Fusion Research

Keywords: electron beam, EEDF, silver reduction, titanium dioxide

DOI: 10.1585/pfr.19.1406004

## 1. Introduction

Silver-titanium dioxide (Ag-TiO<sub>2</sub>) nanostructures have attracted increasing attention due to their unique functional properties and potential applications in many areas such as medicine [1], self-cleaning coatings [2] and photocatalysis [3]. The nanometer-scale structure of supported noble metals is more desirable than the homogeneously coated counterparts due to the larger active sites and therefore higher catalytic performance [4]. The introduction of noble metals to the TiO<sub>2</sub> surface enhances its photocatalytic activity by forming a Schottky barrier that acts as an electron trap to promote interfacial charge transfer, which delays the recombination of the electron-hole pairs [5]. Since heterogeneous photocatalysis is primarily a surface phenomenon, significant efforts have been made to tailor the shape, size, composition, and functionality of the catalyst [6–8]. Conventional methods for synthesizing Ag-TiO<sub>2</sub> nanostructures include the following processes: impregnation [9], sol-gel [10], hydrothermal [11], and photodeposition [12]. However, these synthesis routes involve harmful chemical-reducing agents and high operating temperatures, which could make the process energy-intensive. Therefore, alternative reduction methods have been explored [13].

Several studies utilizing electron-based metal ion reduction methodologies have been reported [14]. Methods include electron beam irradiation [15–19] and electron-assisted reduction using glow discharge as the source of

electrons [3, 20–22]. The mechanism for electron-assisted reduction reactions is not yet very clear due to the difficulty in the characterization of electrons and other active species within cold plasmas [14]. For the electron beam-assisted reduction method, on the other hand, the catalyst precursors are bombarded with high-energy electrons up to 10 MeV with a spot size that varies from the nanometer to the micrometer range [16, 18, 19].

In this work, the low-energy electron beam irradiation method was utilized for the reduction of Ag compound to metallic Ag. A layer of silver nitrate (AgNO<sub>3(aq)</sub>) was prepared on the surface of sputter-deposited TiO<sub>2</sub> films and subsequently exposed to a broad low-energy electron beam, thereby producing Ag-TiO<sub>2</sub> heterostructures [3]. The advantage of using a low-energy electron beam for the reduction of the Ag compound to its metallic state compared to the use of high-energy electrons is its suitability for heat-sensitive substrates and high-energy sensitive samples that could easily undergo electrical charge up. In addition, extracting a broad beam of electrons allows one to treat samples with larger surface areas. The control of electron energy through the extraction electrodes may enable better control of the morphology and efficiency of the reduction process. The surface morphological, structural, and optoelectronic properties of the Ag-TiO<sub>2</sub> films were investigated and correlated with the characteristics of the electron beam. Varying the neutral gas pressure should affect the beam; that is, a higher pressure can create a denser plasma and the electron beam energy may differ when it

author's e-mail: cyjg2301@mail4.doshisha.ac.jp

passes through the produced plasma. Thus, we also report the results as we change the operating pressure of the system.

## 2. Materials and Methods

### 2.1 Experimental system

The effect of electron bombardment on Ag metal formation on the surface of  $\text{AgNO}_3$ -covered  $\text{TiO}_2$  was investigated by extracting a broad electron beam through a pair of mesh electrodes. For this experiment, a custom-designed system (Fig. 1) with an upstream and a downstream chamber separated by extraction electrodes was used [23]. The upstream chamber, where plasma is produced, is made of a water-cooled cylindrical stainless steel (SS) with an inner diameter ( $d$ ) of 86 mm and a height of 82 mm. Samarium-Cobalt (Sm-Co) magnets, with a maximum surface magnetic flux density of approximately 3660 Gauss, were arranged in an octupole configuration outside the body of the chamber. For the hot cathode, two 100 mm long ( $d = 0.3$  mm) tungsten (W) wires were fixed on a current feedthrough and resistively heated to thermionic electron emission. To produce a quiescent discharge, the discharge voltage ( $V_d$ ) and the discharge current ( $I_d$ ) were maintained at 50 V and 100 mA, respectively. That is, the filament current is adjusted to control the filament temperature to achieve  $I_d = 100$  mA limited by the thermionic electron emission current keeping  $V_d = 50$  V. The downstream chamber, where the extracted charged species are collected, has several ports that can be used for beam diagnostics. It is connected to a 150 L/s turbomolecular pump

(ULVAC UTM-150) backed by a rotary pump (ULVAC GLD 136C) to evacuate the system to a base pressure. The pressure of the system was monitored by a cold cathode gauge (CC-10: Tokyo Electronics Co., Ltd.). Between the upstream and downstream chambers is a two-electrode extraction system composed of the powered electrode and grounded electrode separated by a spacer made of a polymeric material. The mesh-like extraction electrodes are made of  $d = 0.1$  mm W wires. The wires are arranged parallel to each other with a 1 mm spacing to realize a transparency of around 90%. The wires were placed on a stainless steel mount with an aperture  $d = 4$  cm. The gap between the electrodes was maintained at 7 mm. To control the energy of the charged species extracted from the source, an extraction potential ( $\phi_{ext}$ ) was applied on the powered electrode. Electron beam irradiation experiments were carried out at two operating pressures:  $7 \times 10^{-3}$  and 0.01 Pa. The 0.01 Pa pressure was adjusted by introducing 99.999% argon (Ar) into the chamber. These two pressures were chosen as the pressure above  $7 \times 10^{-3}$  Pa maintained a stable discharge. Plasma parameters and electron beam characteristics were investigated with the following plasma diagnostics techniques.

### 2.2 Plasma diagnostics

Charged particle measurement techniques were utilized to characterize the plasma in the upstream chamber and the extracted charged species in the downstream chamber. Langmuir probe experiments were conducted using a W wire with  $d = 0.3$  mm and an exposed length of 3 mm

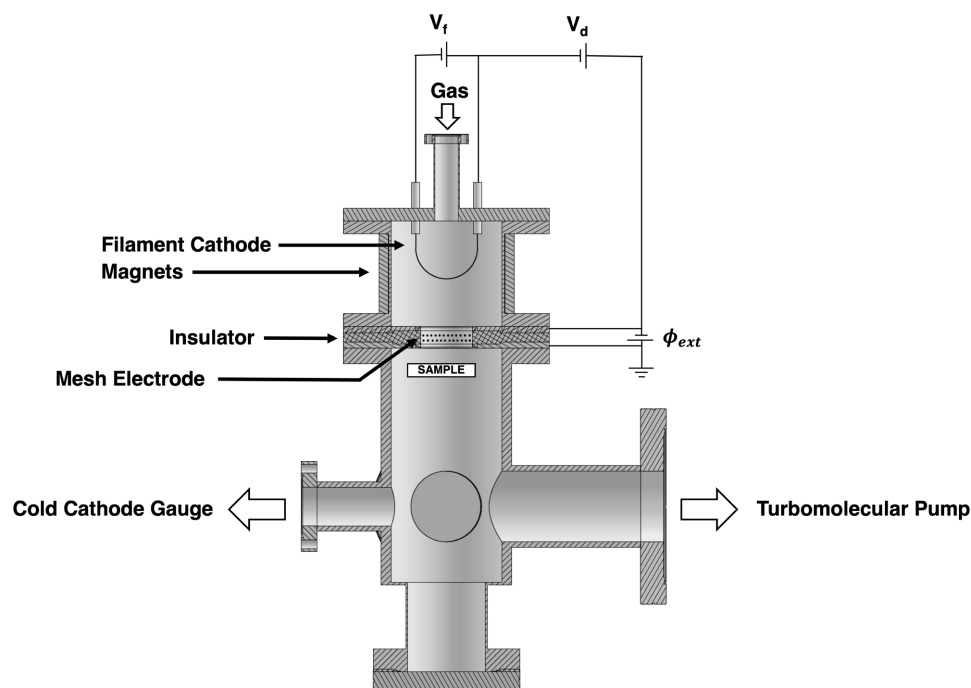


Fig. 1 Schematic of the system used to extract the electron beam.

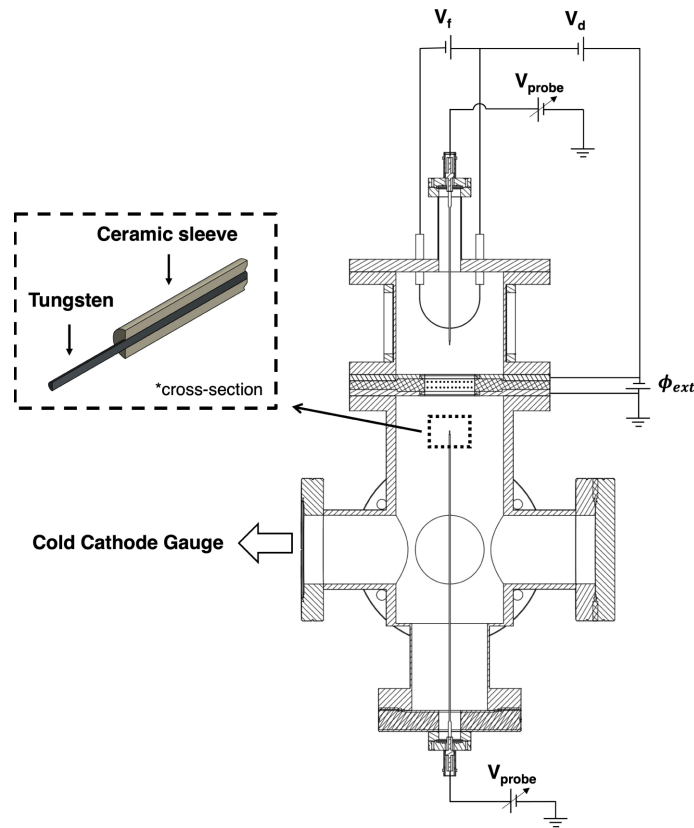


Fig. 2 Schematic diagram of the Langmuir probe.

(Fig. 2). The rest of the wire was electrically insulated with an alumina ( $\text{Al}_2\text{O}_3$ ) ceramic tube.

The upstream probe was positioned 12.5 mm from the upper extraction electrode, while the downstream probe was positioned 11 mm from the lower extraction electrode. A source measure unit (SMU) (Keithley 2614B) was used to obtain the probe current-voltage ( $I$ - $V$ ) characteristics. The probe voltage ( $V_p$ ) was swept from  $-150$  to  $+150$  V. Information on the electron density ( $n_e$ ), electron temperature ( $T_e$ ), and the plasma potential or space potential ( $V_s$ ) were determined from the  $I$ - $V$  characteristics under the assumption of collisionless sheath dynamics around the electrostatic probe.

The current density of the extracted electron beam was measured using a moving Faraday cup (FC) with the inner  $d$  of 10 mm and the height of 21 mm. The electron current that passed through the 0.8 mm  $d$  aperture of the FC shield was measured using a picoammeter (Keithley 6485).

To determine the energy of the extracted electrons, a custom-built retarding potential analyzer (RPA) (Fig. 3) was installed in the downstream region, approximately 10 mm away from the lower extraction electrode. The RPA is made of stainless steel (SS) composed of three plates with an aperture  $d = 0.8$  mm at the center. The topmost plate was floated and used to collimate the beam, the second plate was biased from  $-150$  to  $+30$  V, while the third plate was grounded. The apertures were aligned perpendicular to the direction of the electron beam. The applied

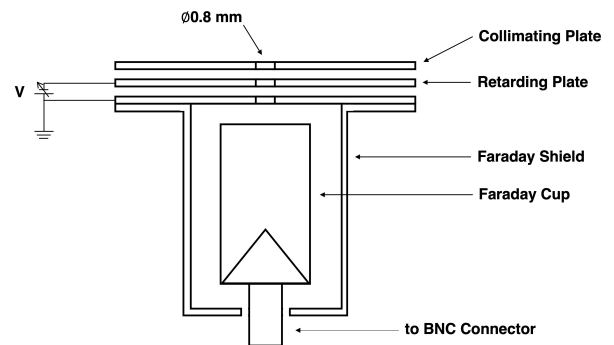


Fig. 3 Schematic of the retarding potential analyzer used in this experiment.

potential acts as an energy filter, allowing electrons with energies greater than the retarding potential to pass through the apertures. Electrons that pass through the apertures are collected by the FC. The electron energy distribution function (EEDF) was estimated from the obtained  $I$ - $V$  trace of the RPA.

### 2.3 Ag-TiO<sub>2</sub> thin film preparation

Before electron beam irradiation, the  $\text{TiO}_2$  films were grown on glass substrates by first depositing a Ti film via sputtering of a Ti target followed by thermal oxidation of the Ti film. The glass substrates were ultrasonically

cleaned in a series of acetone, ethanol, and deionized water baths for 10 min each and subsequently blow-dried using dry air. Ti films were deposited using a custom-built magnetron sputtering system which utilizes a magnetron gun (Torus Mag Keeper, Kurt J. Lesker Co.) with cylindrical and annular magnets. A 2-inch Ti target (99.995%, Kurt J. Lesker Co.) was mounted on the gun using a brass backing plate with a keeper assembly. Plasma can be ignited up to 150 W using a 13.56 MHz radio frequency (RF) power source (ULVAC RFP-N). The system was evacuated to a base pressure of  $7 \times 10^{-4}$  Pa using a 50 L/s turbomolecular pump (ULVAC UTM-50) coupled to a rotary pump (Yamato PD-139). The process gas used was Ar (99.999%, EliteJaz), maintained at 1.0 Pa during deposition. The discharge was allowed to run for 15 min. After deposition, the Ti films were thermally oxidized for 6 h in a furnace (Lenton UAF 16/5) at 550°C with 220 sccm O<sub>2</sub> flow rate. The TiO<sub>2</sub> films were allowed to cool inside the furnace to prevent thermal shock. The TiO<sub>2</sub> films were then submerged in 0.1 M AgNO<sub>3(aq)</sub> solution (99.9%, RTC Laboratory Services & Supply House PH) for 24 h under ambient conditions to introduce Ag cations into the porous TiO<sub>2</sub> film. The films were dried in an electric oven at 100°C for 30 min. The samples were then irradiated with a beam of electrons extracted at  $\phi_{ext} = 100$  V for 0, 5, 10, 20, and 30 min exposure times.

The surface morphological, structural, and optoelectronic properties of the synthesized Ag-TiO<sub>2</sub> films were investigated using different characterization techniques. Raman spectroscopy (Horiba Scientific LabRAM HR Evolution) was used to check the chemical structure and molecular interactions of the films. The samples were posi-

tioned on the stage and exposed to a laser with 532 nm excitation wavelength. The scan range was set from 100 to 1200 cm<sup>-1</sup>. The average bulk composition of the films was determined using X-ray diffraction (XRD) (PANALYTICAL X'Pert PRO) with settings at 0.05 scan step, 1 s scan speed, and range  $20^\circ \leq 2\theta \leq 80^\circ$ . A UV-Vis spectrometer (Hitachi UH5300) was used to check the transmittance of the films. Data were obtained within the spectral range of 300-700 nm at a scan speed of 400 nm/min. The surface morphology was observed through scanning electron microscopy (SEM) (JEOL JSM7001) while the elemental composition of the film was identified through energy dispersive X-ray spectroscopy (EDS) (Hitachi SU8020). Finally, a 4-point probe system (EverBeing SR-4) was used to measure the sheet resistance of the films.

### 3. Results

#### 3.1 Plasma diagnostics

Fundamental plasma parameters can be determined by inserting an electrostatic probe in the region of interest within the discharge [24]. Figure 4 (a) shows representative Langmuir probe *I-V* traces obtained in this experiment. The *I-V* traces showed no evidence of significant fluctuations, suggesting the production of a stable quiescent discharge commonly observed in multi-cusp hot cathode filament systems [25–27].

Table 1 summarizes the plasma parameters obtained in the upstream and downstream chambers at operating pressures of  $7 \times 10^{-3}$  and 0.01 Pa. At  $7 \times 10^{-3}$  Pa, the estimated  $T_e$  for the upstream and downstream regions were 5.2 and 2.5 eV, respectively. When a small amount of Ar

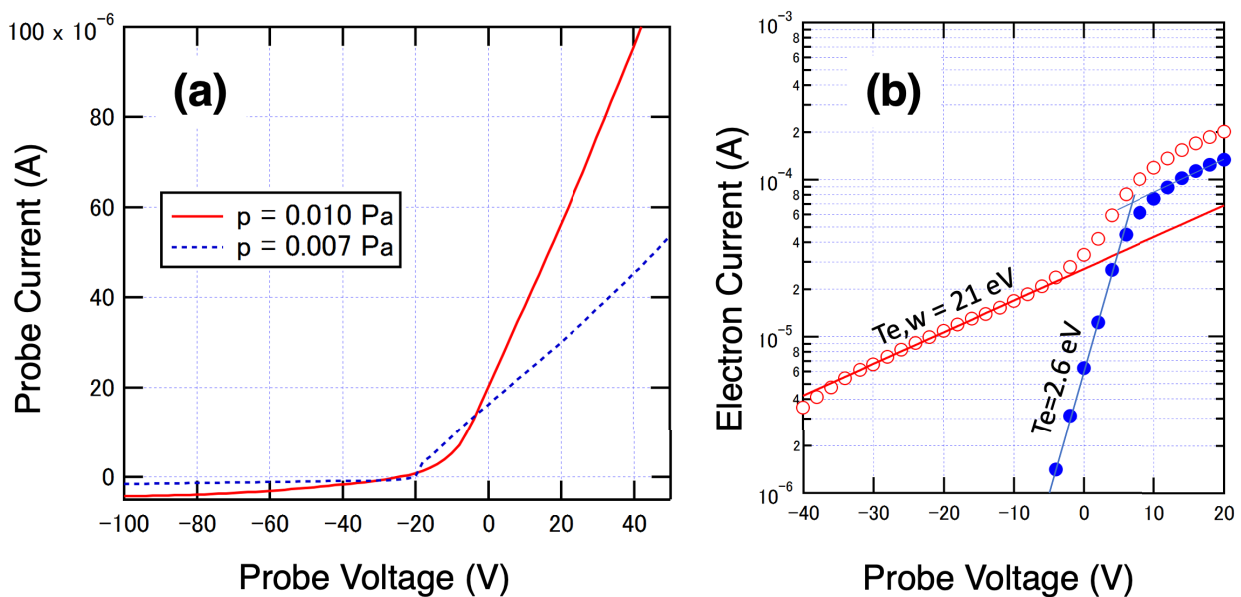


Fig. 4 (a) Representative Langmuir probe *I-V* traces obtained at the downstream region and (b)  $T_e$  values estimated from the logarithmic plot of the electron current for a discharge produced in the upstream region at 0.01 Pa. The operating parameters were set at  $I_d = 100$  mA,  $V_d = 50$  V, and  $\phi_{ext} = 100$  V.

Table 1 Calculated plasma parameters.

Plasma Parameter	Upstream Region		Downstream Region	
	$7 \times 10^{-3}$ Pa	0.01 Pa	$7 \times 10^{-3}$ Pa	0.01 Pa
$V_s$ (V)	-57	7	-4	2.5
$I_{sat}$ (A)	$7.30 \times 10^{-6}$	$1.10 \times 10^{-4}$	$1.02 \times 10^{-5}$	$3.00 \times 10^{-4}$
$T_e$ (eV)	5.2	2.6	2.5	6.5
$T_{e,w}$ (eV)	-	21	-	-
$n_e$ ( $\text{cm}^{-3}$ )	$1.25 \times 10^{13}$	$2.00 \times 10^{14}$	$2.52 \times 10^{13}$	$4.59 \times 10^{14}$

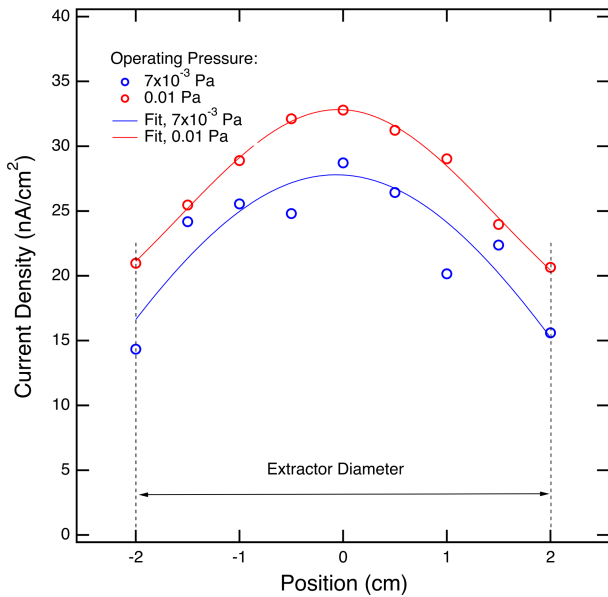


Fig. 5 Profile of the electron beam current density along the diameter of the extraction electrode.

gas was introduced into the system, two regions with constant slopes in the logarithmic plot were recorded for the  $I$ - $V$  trace in the upstream region. At 0.01 Pa, the estimated  $T_e$  were 2.6 and 6.5 eV for the upstream and downstream regions, respectively. Warm electrons ( $T_{e,w}$ ) with the apparent temperature of 21 eV were also detected at 0.01 Pa operating pressure by the probe positioned in the upstream region. Thermalized electrons, which are products of electron impact ionization, have lower energies. Warm electrons, on the other hand, are thermionically emitted from the cathode and therefore have higher energies. At 0.01 Pa, the calculated  $n_e$  increased by one order of magnitude both in the upstream and downstream regions compared to  $7 \times 10^{-3}$  Pa despite only 42% increase in the operating pressure. It can also be observed that when the system was operated with the gas pressure set to 0.01 Pa, a positive  $V_s$  was achieved.

The current density profile of the electron beam extracted at  $\phi_{ext} = 100$  V was measured using a moving FC placed in the downstream region. Figure 5 shows the spatial distribution of the electron beam current density along the diameter of the extraction electrode. At the cen-

ter of the beam ( $x = 0$ ),  $32 \text{ nA/cm}^2$  current density was measured when the system was operated at 0.01 Pa. At  $7 \times 10^{-3}$  Pa operating pressure, the measured current density was  $28 \text{ nA/cm}^2$  at the same position. The higher current density measured when more Ar was introduced into the system was due to the presence of thermalized electrons in addition to the electrons extracted directly from the thermionically heated filament. Without a background gas, the space charge of the electrons could contribute to the divergence of the beam, thus also reducing the current density. The presence of  $\text{Ar}^+$ , on the other hand, can provide neutralization of the space charge of the electrons, minimizing the beam divergence and thus having a higher current density, as seen in Fig. 5.

In Fig. 5, the electron current density data showed scattering when the system was operated at  $7 \times 10^{-3}$  Pa Ar pressure. The fluctuations in the measured electron beam current density profile along the diameter of the electrode aperture can be attributed to the space charge in front of the FC shield surface, as described later. However, these effects may be negligible to estimate the overall spatial profile of the electron current density.

To examine the energy of the electron beam extracted in the downstream region, a custom-built RPA was used. This technique uses a series of electrostatic plates positioned in front of a current-collecting surface to selectively allow the passage of charged species depending on the potential induced on the retarding plate. In Fig. 6, the energy of the extracted electron is estimated to be around  $-30$  eV at  $7 \times 10^{-3}$  Pa operating pressure. Upon the introduction of Ar up to 0.01 Pa, the beam energy was estimated to be  $-100$  eV, which is equal to the applied  $\phi_{ext}$ . Additionally, a broad peak from  $-20$  to  $20$  eV was observed, which could be attributed to thermalized electrons produced in the downstream region. For both pressure conditions, the energy spreads were estimated to be 11 V, which is narrow enough compared with the beam energy. The small amount of gas added to the system did not appear to affect the energy spread of the beam. The beam spatial distributions also did not differ much.

### 3.2 Ag-TiO<sub>2</sub> thin film characterization

Raman spectroscopy is a technique used to identify the molecular structure of samples through their vibra-

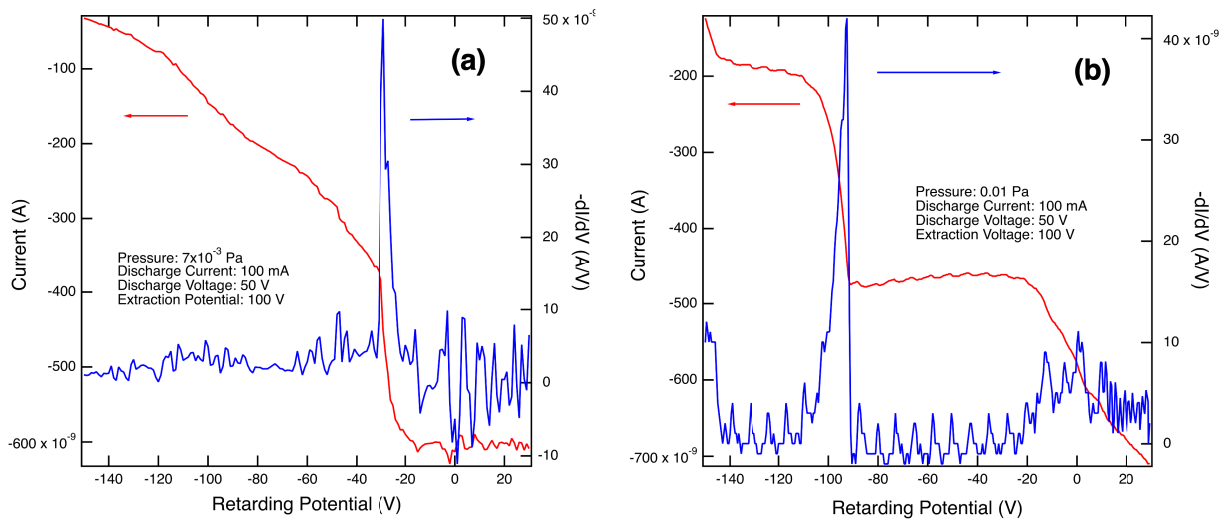


Fig. 6 *I-V* traces and corresponding electron energy distribution functions measured by a retarding potential analyzer at (a)  $7 \times 10^{-3}$  Pa and (b) 0.01 Pa operating pressure.

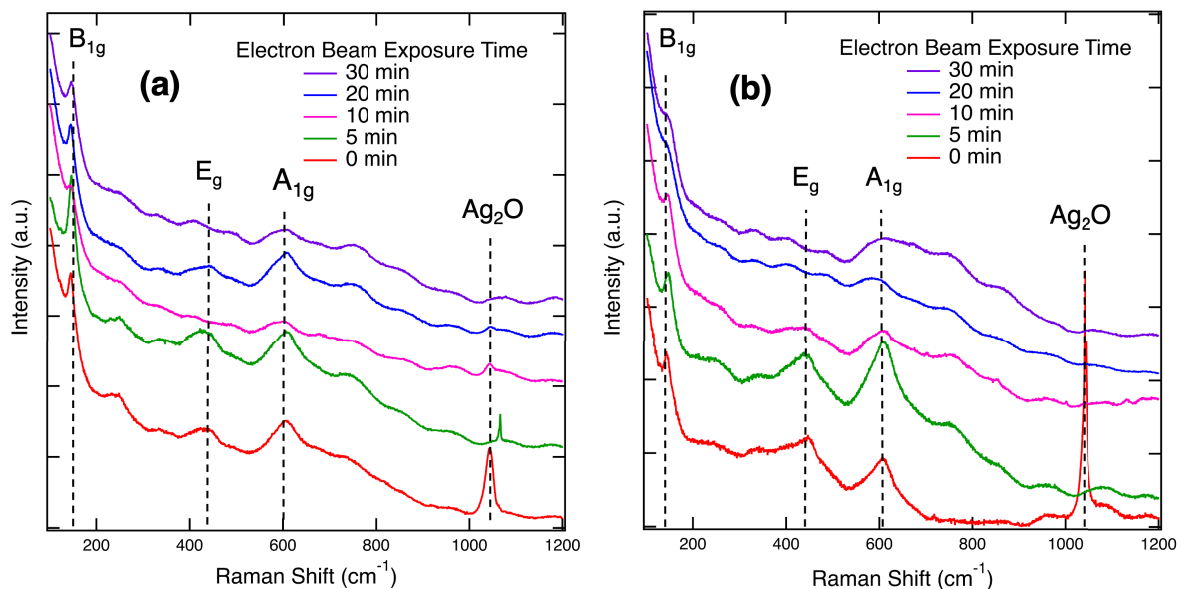


Fig. 7 Raman spectra of Ag-TiO<sub>2</sub> films irradiated with an electron beam extracted at (a)  $7 \times 10^{-3}$  Pa and (b) 0.01 Pa.

tional and rotational energy modes. Raman spectra for samples prepared at varying electron beam exposure times and operating pressures are shown in Fig. 7.

The synthesized TiO<sub>2</sub> matrix was in rutile phase, as confirmed by the three Raman active modes of rutile expressed as B<sub>1g</sub>, E<sub>g</sub>, and A<sub>1g</sub> from the observed peaks at 145, 446, 610 cm<sup>-1</sup>, respectively [28]. The Raman peak of Ag<sub>2</sub>O centered at 1044 cm<sup>-1</sup> [29] was also observed for some of the samples. As the exposure time of the electron beam is increased, the peak of Ag<sub>2</sub>O disappears. In general, the peaks at higher wavenumbers disappear from 10 min of electron beam exposure. This suggests the formation of metallic Ag on the surface of the film as metals do not show changes in polarizability during molecular

vibrations; hence, the characteristic Raman peaks of the metal oxides become undetectable.

The conversion of the Ag precursor to metallic Ag by electron beam irradiation was further assessed through XRD. Figure 8 shows the XRD spectra of the Ag-TiO<sub>2</sub> films as a function of the electron beam exposure time at  $7 \times 10^{-3}$  and 0.01 Pa operating pressures.

For the Ag-TiO<sub>2</sub> samples prepared at  $7 \times 10^{-3}$  Pa, the intensity of the peak at 32° corresponding to Ag<sub>2</sub>O (111) [30] decreases as new peaks at ~38° corresponding to Ag (111) [31] appear at longer electron beam exposure times. For the samples prepared at 0.01 Pa, the peak of Ag (111) was also detected. For this setting, no trend can be observed in the peak intensity as a function of exposure time.

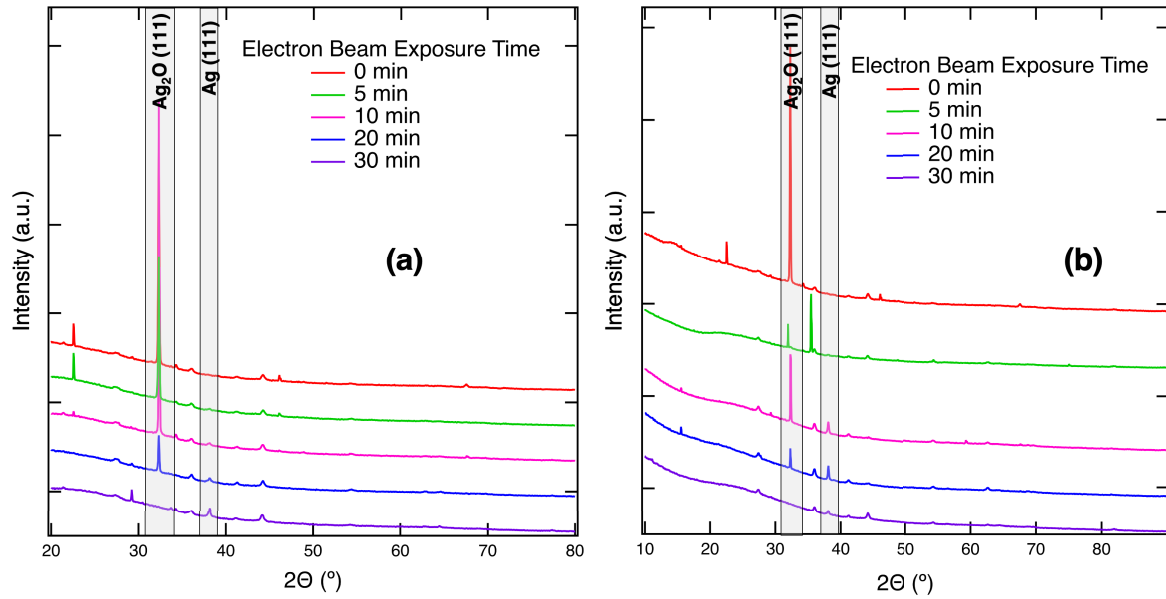


Fig. 8 X-ray diffractograms of Ag-TiO<sub>2</sub> films irradiated with electron beam extracted at (a)  $7 \times 10^{-3}$  and (b) 0.01 Pa.

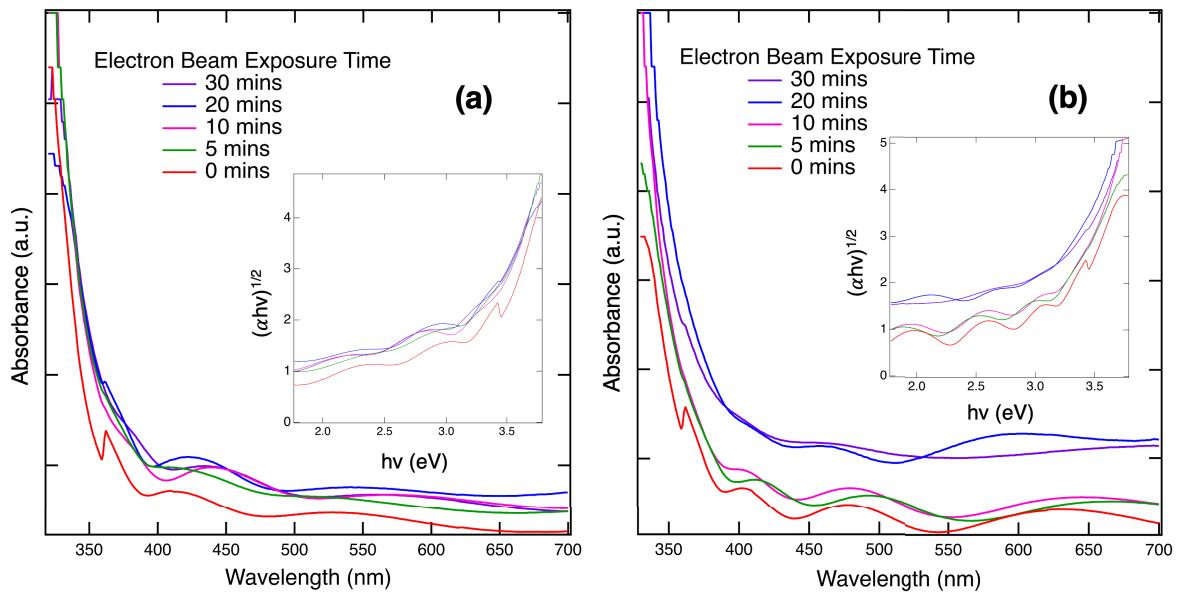


Fig. 9 UV-vis spectra of Ag-TiO<sub>2</sub> films irradiated with electron beam extracted at (a)  $7 \times 10^{-3}$  and (b) 0.01 Pa. Inset: Tauc plots generated from the UV-vis spectra.

The absorbance of the films was obtained using UV-Vis spectroscopy. Shown in Fig. 9 are the absorbance spectra at wavelengths ranging from 320 to 700 nm. The onset of the UV absorption edge can be observed at around 350 nm for all the samples prepared at  $7 \times 10^{-3}$  Pa (Fig. 9(a)). The onset of the UV absorption edge for the samples prepared at 0.01 Pa (Fig. 9(b)) is also at 350 nm. However, a slight shift of the absorption edge to longer wavelengths can be observed for samples prepared at 0.01 Pa and irradiated with an electron beam for 20 and 30 min.

The UV-Vis absorbance spectra were used to estimate

the optical bandgap ( $E_g$ ) of the Ag-TiO<sub>2</sub> films. Plots of  $\alpha hv$  were calculated using the Tauc Eq. (1):

$$\alpha hv = A(hv - E_g)^n, \quad (1)$$

where  $A$  is a constant,  $hv$  is the photon energy,  $E_g$  is the allowed energy gap, and  $n$  is a constant ( $\frac{1}{2}$  for direct transitions) [32].

Tauc plots are shown as insets of Fig. 9, while Table 2 summarizes the calculated  $E_g$  values of Ag-TiO<sub>2</sub> films. Samples not irradiated with an electron beam had the highest  $E_g$  at 3.27 and 3.13 eV for  $7 \times 10^{-3}$  and 0.01 Pa operating pressure, respectively. Although Ag-TiO<sub>2</sub> films

that were irradiated with the electron beam can be observed to exhibit slightly lower  $E_g$  values, in general, there were no significant changes in the band gap. The average  $E_g$  was calculated to be 3.06 eV and 3.03 eV for the Ag-TiO<sub>2</sub> films prepared at  $7 \times 10^{-3}$  and 0.01 Pa, respectively, which are close to the reported  $E_g$  of rutile TiO<sub>2</sub> at 3.02 eV [33].

Table 2 Calculated  $E_g$  from the Tauc plots.

Exposure Time (min)	$E_g$ (eV)	
	$7 \times 10^{-3}$ Pa	0.01 Pa
0	3.27	3.13
5	2.97	2.98
10	3.07	3.11
20	3.00	2.97
30	3.01	2.96

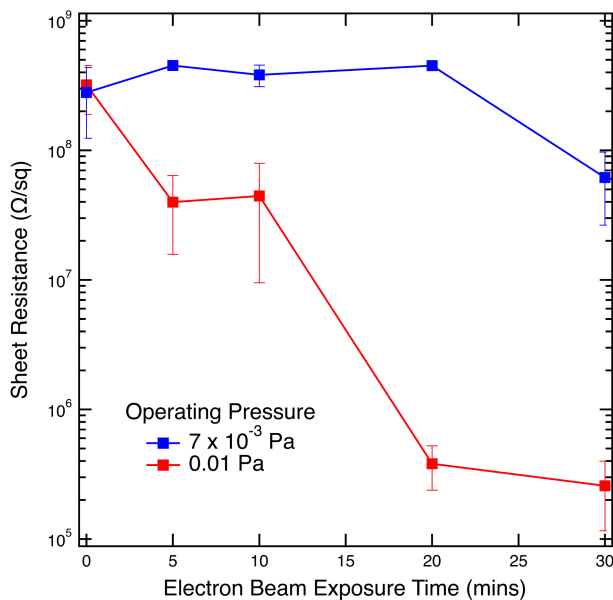


Fig. 10 Sheet resistance measurements of Ag-TiO<sub>2</sub> films irradiated with electron beam extracted at  $7 \times 10^{-3}$  and 0.01 Pa.

Figure 10 shows the sheet resistance measurements for the samples irradiated with an electron beam at varying exposure times. Before exposure to the electron beam, the measured resistance values were  $2.8 \times 10^8$  and  $3.2 \times 10^8$  Ω/sq for the samples prepared at  $7 \times 10^{-3}$  and 0.01 Pa, respectively. After 30 min of electron beam exposure, the sheet resistance of the sample prepared at  $7 \times 10^{-3}$  Pa decreased to  $6.2 \times 10^7$  Ω/sq while the samples prepared at 0.01 Pa decreased to  $2.6 \times 10^5$  Ω/sq.

SEM and EDS were used to probe the surface morphology and confirm the elemental composition of the Ag-TiO<sub>2</sub> film. Figure 11 shows a representative electron image and the corresponding elemental maps that indicate the presence of Ag and O. In the overlay (Fig. 11 (b)), the areas that correspond to Ag did not have O signals, suggesting the metallic nature of the material.

## 4. Discussion

Electrons play an important role in catalyst preparation by direct surface reactions. Recombination events occur, which allow the reduction of metal ions from metal catalyst precursors to their metallic state [19, 22, 34, 35]. The present work demonstrated the extraction of a broad low-energy electron beam to induce the reduction of Ag metal from a metal salt precursor (AgNO<sub>3</sub>) on TiO<sub>2</sub> film matrix. The films irradiated with an electron beam exhibited Ag metal peaks, as observed in the X-ray diffractograms for both operating pressures. The Raman spectra of the films also suggested the conversion to Ag metal as a result of the disappearance of the Ag oxide peaks with an increasing electron beam irradiation time. While samples prepared at  $7 \times 10^{-3}$  Pa had higher sheet resistance values compared to samples prepared at 0.01 Pa operating pressure, the sheet resistance decreases as a function of the electron beam treatment dose. The decrease in resistance is attributed to the presence of Ag metal on the surface, which contributes to an increase in the conductivity of the film, forming a larger patch of metallic Ag. The  $E_g$  energies of the films were estimated through Tauc plots. A shift of the absorption edge to longer wavelengths was observed for the films exposed to electron beam. The lowest

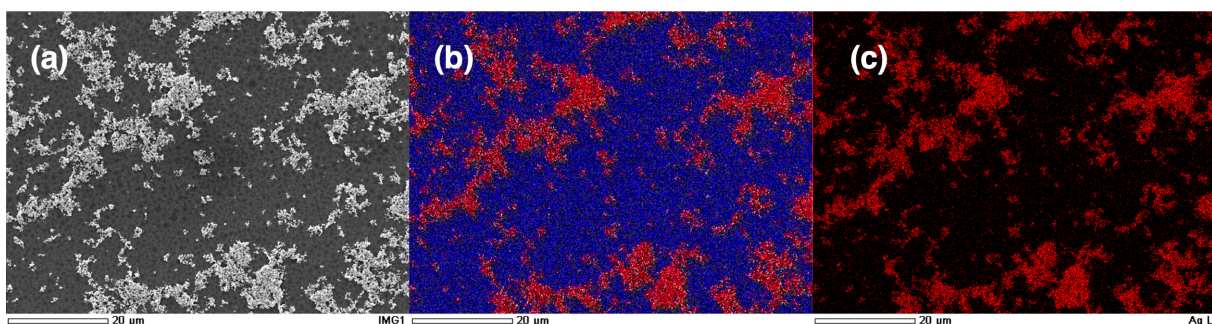


Fig. 11 (a) SEM image of the Ag-TiO<sub>2</sub> film and corresponding EDS maps for (b) Ag (red) and O (blue) overlay, and (c) Ag.

$E_g$  was estimated to be 2.96 eV for Ag-TiO<sub>2</sub> films exposed to 30 min of electron beam extracted at 0.01 Pa operating pressure.

The difference in the film properties can be explained by the difference in the beam energy distribution function observed when the extraction was done with and without a background gas. The electron energy was higher under higher Ar pressure conditions and therefore improved the formation of Ag metal on the surface of TiO<sub>2</sub>. The effectiveness of beam energy on metallic Ag formation can be confirmed in Fig. 10, which indicates the saturation of the reaction with a much lower exposure dose for 0.01 Pa pressure. With the introduction of a small amount of gas, the beam has an energy equal to the applied  $\phi_{ext}$  at 100 V. Meanwhile, with a smaller background gas pressure, the beam component possessed only 30 V kinetic energy. This resulted in the reduction reaction proceeding slowly.

The mechanism of losing the beam energy at  $7 \times 10^{-3}$  Pa pressure was investigated through measuring the plasma parameters with Langmuir probes. Above  $7 \times 10^{-3}$  Pa, thin ion sheath region is created around the discharge filament in a stable plasma with enough Ar density. The mean free path for electron impact ionization exceeds  $2 \times 10^3$  cm below  $7 \times 10^{-3}$  Pa based upon the Ar ionization cross section data [36], and the ionization events become extremely low in the downstream chamber. The measured data suggests that the electron density is one order of magnitude lower from the condition at 0.01 Pa, despite only 42% increase in pressure. The plasma potential is negative for  $7 \times 10^{-3}$  Pa meaning electrons forming negative space charge in both upstream and downstream region. That is, ionization was not promoted enough to let the plasma flow to be ambipolar and ion productions both upstream and downstream are inadequate to form a plasma without electric field. The density of electrons in the upstream chamber is small, while the electrons penetrating the downstream region of the extractor comes into the RPA. As the space potential in the region where these electrons are produced must be less than 100 V, the RPA showed the energy distribution function peaked at an energy lower than the 100 V extraction potential. The measured space potential in the downstream chamber was  $-4$  V and was smaller in magnitude than  $-30$  V. While the probe measured the  $I$ - $V$  characteristics, the RPA was removed from the system. The effect due to secondary electron emission from the front plate of the RPA can be an additional source of electrons producing more negative space potential to raise the peak electron energy up to 30 eV.

## 5. Conclusions

Ag-TiO<sub>2</sub> films were synthesized through electron beam-induced reduction of Ag metal salt precursor on sputter-deposited TiO<sub>2</sub> films. Electron beams with energies of 100 and 30 eV were extracted and utilized in the reduction process. The current density increased from

28 to 32 nA/cm<sup>2</sup> upon the introduction of 0.01 Pa Ar into the system. SEM and EDS confirmed the formation of metallic Ag, which is attributed to the decomposition of the Ag compound by the electron beam. The X-ray diffractograms and Raman spectra also confirmed the formation of electron-beam-reduced metallic Ag. It is evident that the exposure time, current density, and electron beam energy influenced the structural and optoelectronic properties of the film. In particular, the samples prepared at 0.01 Pa exhibited lower  $E_g$  and sheet resistance values compared to the samples prepared at  $7 \times 10^{-3}$  Pa. This work demonstrated the capability of low-energy electrons to reduce noble metals from their compounds. It also showed that a low downstream pressure can form a plasma with a negative space charge, indicating that an electron beam is formed to irradiate the surface but the energy is much smaller than the extraction potential. Injecting a small amount of gas may help the system create an electron beam with full extraction energy.

## Acknowledgments

The authors acknowledge the UP Diliman Micro-fabrication Facility for the use of the 4-point probe and the nanoQuench project (CHED PCARI IIID-2016-007) for the use of the Raman Spectrometer. A. Montallana acknowledges the Yoshida Scholarship Foundation. M. Vasquez acknowledges the DOST-PCIEERD Project No. 03058, the University of the Philippines Office of the Vice President for Academic Affairs BALIK-PhD Research Grant (OVPA-BPhD-2014-01) and the Felix M. Gonzalez Professorial Chair in Materials Engineering.

- [1] S. Jalali *et al.*, J. Taiwan Inst. Chem. Eng. **66**, 357 (2016).
- [2] X. Yang *et al.*, J. Nanopart. Res. **16**, 2526 (2014).
- [3] A. Montallana *et al.*, J. Vac. Sci. Technol. B **41**, 042204 (2023).
- [4] H. Kim *et al.*, Plasma Chem. Plasma Process. **36**, 45 (2016).
- [5] A. Chauhan *et al.*, Appl. Phys. Rev. **5**, 041111 (2018).
- [6] S. Dong *et al.*, RSC Adv. **5**, 14610 (2015).
- [7] M. Rastogi *et al.*, Mater. Sci. Semicond. **51**, 33 (2016).
- [8] P. Kamat, Acc. Chem. Res. **50**, 527 (2017).
- [9] B. Naik *et al.*, J. Exp. Nanosci. **8**, 462 (2013).
- [10] S. Abbad *et al.*, J. Environ. Chem. Eng. **8**, 103718 (2020).
- [11] X. Zheng *et al.*, Inorg. Chem. Commun. **110**, 107589 (2019).
- [12] K. Wenderich *et al.*, Chem. Rev. **116**, 14587 (2016).
- [13] R. White *et al.*, Chem. Soc. Rev. **38**, 481 (2009).
- [14] C. Liu *et al.*, Chinese J. Catal. **37**, 340 (2016).
- [15] Y. Ohkubo *et al.*, J. Mater. Sci. **48**, 5047 (2013).
- [16] S. Seino *et al.*, J. Nanopart. Res. **10**, 1071 (2008).
- [17] Y. Pai *et al.*, J. Power Sources **159**, 878 (2006).
- [18] K. Song *et al.*, ACS Catal. **2**, 384 (2012).
- [19] J. Kugai *et al.*, Appl. Catal. B: Environ. **126**, 306 (2012).
- [20] J. Zou *et al.*, Langmuir **22**, 11388 (2006).
- [21] M. Darwish *et al.*, Green Chem. **24**, 8142 (2022).
- [22] A. Osonio and M. Vasquez, Appl. Surf. Sci. **432**, 156 (2018).

- [23] M. Vasquez *et al.*, *Vacuum* **187**, 110067 (2021).
- [24] F. Chen, IEEE-ICOPS Meeting, Jeju, Korea Volume 2.
- [25] K. Ehlers *et al.*, *Rev. Sci. Instrum.* **53**, 1429 (1982).
- [26] A. Patel *et al.*, *Rev. Sci. Instrum.* **89**, 043510 (2018).
- [27] M. Vasquez *et al.*, *Rev. Sci. Instrum.* **85**, 02A717 (2013).
- [28] F. Hardcastle, *Journal of the Arkansas Academy of Science* **65**, 43 (2011).
- [29] G. Waterhouse *et al.*, *Phys. Chem. Chem. Phys.* **3**, 3838 (2001).
- [30] Z. Dhoondia *et al.*, *J. Nanosci. Nanotechnol.* **2**, 15 (2012).
- [31] Y. Sui *et al.*, *J. Vac. Sci. Technol. A* **36**, 051302 (2018).
- [32] P. Makula *et al.*, *J. Phys. Chem. Lett.* **9**, 6814 (2018).
- [33] Y. Nosaka *et al.*, *J. Phys. Chem. Lett.* **7**, 431 (2016).
- [34] C. Liu *et al.*, *ACS Sustain. Chem. Eng.* **2**, 3 (2014).
- [35] Z. Wang *et al.*, *ACS Catal.* **8**, 2039 (2018).
- [36] S.C. Brown, *Basic Data of Plasma Physics: The Fundamental Data on Electrical Discharges in Gases* (American Institute of Physics, 1997).